Indirect measurements of neutron-induced reaction cross sections at heavy-ion storage rings

M. Sguazzin[1], B. Jurado[1,*], J. Pibernat[1], J. A. Swartz[1], M. Grieser[2], J. Glorius[3], Yu. A. Litvinov[3], R. Reifarth[4], K. Blaum[2], P. Alfaurt[1], P. Ascher[1], L. Audouin[5], C. Berthelot[1], B. Blank[1], B. Bruckner[4], S. Dellmann[4], I. Dillmann[6], C. Domingo-Pardo[7], M. Dupuis[8,9], P. Erbacher[4], M. Flayol[1], O. Forstner[3], D. Freire-Fernández[2,10], M. Gerbaux[1], J. Giovinazzo[1], S. Grévy[1], C. J. Griffin[6], A. Gumberidze[3], S. Heil[4], A. Heinz[11], D. Kurtulgil[4], G. Leckenby[6], S. Litvinov[3], B. Lorentz[3], V. Méot[8,9], J. Michaud[1], S. Perard[1], N. Petridis[3], U. Popp[3], D. Ramos[12], M. Roche[1], M.S. Sanjari[3], R.S. Sidhu[13], U. Spillmann[3], M. Steck[3], Th. Stöhlker[3], B. Thomas[1], L. Thulliez[14] and M. Versteegen[1]

[1]LP2I Bordeaux, CNRS/IN2P3-Université de Bordeaux, 33170 Gradignan, France
[2]Max-Planck Institut für Kernphysik, 69117 Heidelberg, Germany
[3]GSI Helmholtzzentrum für Schwerionenforschung, 64291 Darmstadt, Germany
[4] Goethe University of Frankfurt, 60438 Frankfurt, Germany
[5] Université Paris-Saclay, CNRS, IJCLab, 91405 Orsay, France
[6]TRIUMF, Vancouver, British Columbia, V6T 2A3, Canada
[7]IFIC, CSIC-Universidad de Valencia, 46980 Valencia, Spain
[8]CEA, DAM, DIF, 91297 Arpajon, France
[9]Université Paris-Saclay, CEA, Laboratoire Matière sous Conditions Extrêmes, 91680 Bruyères-Le-Châtel, France
[10]Ruprecht-Karls-Universität Heidelberg, 69117 Heidelberg, Germany
[11]Chalmers University of Technology, 41296 Gothenburg, Sweden
[12]GANIL, 14000 Caen, France
[13]School of Physics and Astronomy, University of Edinburgh, UK
[14] CEA-Paris Saclay, 91191 Gif-sur-Yvette, France

Abstract. Neutron-induced reaction cross sections of unstable nuclei are essential for understanding the synthesis of heavy elements in stars and for applications in nuclear technology. However, their measurement is very complicated due to the radioactivity of the targets involved. We propose to circumvent this problem by using the surrogate reaction method in inverse kinematics, where the nucleus formed in the neutron-induced reaction of interest is produced by a reaction involving a radioactive heavy-ion beam and a stable, light target nucleus. The probabilities as a function of the compound-nucleus excitation energy for γ-ray emission, neutron emission and fission, which can be measured with the surrogate reaction, are particularly useful to constrain model parameters and to obtain more accurate predictions of the neutron-induced reaction cross sections of interest. Yet, the full development of the surrogate method is hampered by numerous long-standing target issues, which can be solved by combining surrogate reactions with the unique and largely unexplored possibilities at heavy-ion storage rings. In this contribution, we describe the developments we are carrying out to measure for the first time simultaneously γ-ray emission, neutron emission and fission probabilities at the storage rings of the GSI/FAIR facility. In particular, we will present the first results of the proof of principle experiment, which we performed in June 2022 at the Experimental Storage Ring (ESR) of GSI/FAIR.

1 Introduction

Most of the elements from iron to uranium are synthesized in stars via neutron-induced reactions during the slow (s) and rapid (r) neutron-capture processes. The detection of gravitational waves from the merger of two neutron stars [1], and the subsequent kilonova, consistent with being powered by the radioactive decay of nuclei synthesized by the r-process [2, 3], demonstrated that neutron-star mergers are an important r-process site. Still, many uncertainties and open questions remain regarding the r-process. For instance, it is not yet clear if the r-process abundance distribution in the solar system is the result of one or multiple scenarios. The measurement of neutron-induced cross sections of key neutron-rich nuclei is essential to answer this question [4]. In the neutron-star merger scenario, the fission process plays a significant role [4, 5, 6, 7]. The r-process is terminated at extremely neutron-rich nuclei in the actinide region undergoing fission. Fission recycling can then occur where the produced fission fragments continue to undergo neutron captures and β decays until fission again terminates the r-process path. After a few cycles, the abundances in the

* Corresponding author: jurado@cenbg.in2p3.fr

mass region 120 < A < 210 can become dominated by the fission-fragment distributions.

Neutron-induced cross sections of radioactive nuclei are also crucial ingredients for the simulation of advanced nuclear systems for the transmutation of nuclear waste or for the development of innovative fuel cycles like the thorium cycle [8].

1.1 Neutron-induced reactions

A neutron-induced reaction at incident energies below a few MeV can be mainly described as a two-step process (Fig. 1). In the first step, the nucleus A captures the neutron forming a compound nucleus (A+1)*. The excited compound nucleus can then decay in different ways: (i) by emitting γ-rays, this is the radiative neutron capture reaction (n,γ); (ii) by emitting a neutron, leaving the mass number A and the proton number Z of the nucleus unchanged, this is denoted as elastic (n,n) or inelastic scattering (n,n'); (iii) by fission, (n,f), if the compound nucleus is heavy enough. Each decay mode has a given probability (P_{γ}, P_{n}, P_{f}) and the sum of the probabilities of all the possible decay channels must be 1.

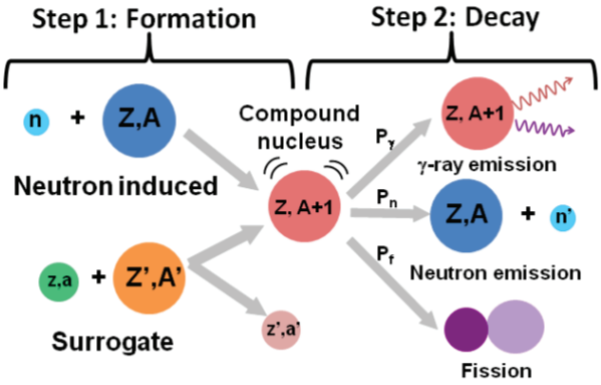

Fig. 1. Sequence of a neutron-induced reaction. First a compound nucleus is formed, which then de-excites by the emission of γ -rays, a neutron or by fission. The probability P associated to each decay channel is indicated. In a surrogate reaction, the same compound nucleus as in the neutron-induced reaction is produced by a different reaction, namely a two-body reaction such as an inelastic-scattering or a transfer reaction.

In traditional neutron-irradiation experiments, the direct measurement of neutron-induced cross sections of short-lived nuclei is very challenging because of the difficulties to produce and handle radioactive targets. Moreover, the associated radioactivity can generate a significant background, which is very difficult to distinguish from the signals originating from the decay of the nucleus (A+1)* and can damage the detectors during the measurement.

When the target nuclei are highly radioactive, experimental data are scarce and most of the neutron-induced reaction cross sections rely on theoretical model predictions. However, these predictions often have very large uncertainties due to difficulties in describing the compound-nucleus de-excitation process (step 2 in Fig. 1). Indeed, the de-excitation process is ruled by fundamental properties (level densities, fission barriers, transmission coefficients, etc.) for which the existing nuclear models give very different predictions. This leads to discrepancies between the calculated cross sections as large as two orders of magnitude or more when no experimental data are available [9].

1.2 Surrogate reactions

It is possible to overcome the radioactive-target difficulties described above by performing the experiments in inverse kinematics with radioactive ion beams. However, this is not yet possible for neutron-induced reactions since free neutron targets are not available. An alternative to infer neutron-induced reaction cross sections is to use the surrogate-reaction method in inverse kinematics. The surrogate reaction produces the compound nucleus of interest by a different reaction than the neutron-induced reaction (see Fig. 1) and the decay probabilities for fission, γ and neutron emission are measured as a function of the excitation energy of the compound nucleus. The measured decay probabilities are used to constrain model parameters (fission barriers, particle transmission coefficients, level densities, etc.) and enable much more accurate predictions of the desired neutron-induced reaction cross sections.

In the Hauser-Feshbach (HF) statistical reaction formalism [10], the decay probabilities $P_{i,\chi}$ obtained with the surrogate (i=s) and the neutron-induced (i=n) reactions are given by:

$$P_{i,\chi}(E^*) = \sum_{J^\pi} F_i(E^*, J^\pi) \cdot G_\chi(E^*, J^\pi) \quad (1)$$

where $F_i(E^*, J^\pi)$ are the probabilities to form the excited nucleus in a state with spin J and parity π at an excitation energy E* by the corresponding reaction, and $G_\chi(E^*, J^\pi)$ are the probabilities that the nucleus decays from that state via decay channel χ (γ-emission, neutron emission or fission). The factorized form in eq. (1) reflects the essential assumption of the HF model that a compound nucleus (CN) is formed, whose decay is independent of the way it was formed [10]. At a sufficiently high E* the Weisskopf-Ewing (WE) limit applies, i.e. the probabilities G_χ become independent of J^π [11], thus $P_{s,\chi} \approx P_{n,\chi}$ and one may infer the neutron-induced cross section $\sigma_{n,\chi}$ by applying:

$$\sigma_{n,\chi}(E_n) \cong \sigma_{CN}(E_n) \cdot P_{s,\chi}(E^*) \quad (2)$$

where $\sigma_{CN}(E_n)$ is the cross section for the formation of a CN after the capture of a neutron of energy E_n. σ_{CN} can be calculated with the optical model with an uncertainty of about 5 % for nuclei near the valley of stability [11]. E_n and E* are related via the relation $E_n=[(A+1)/A]\cdot(E^*-S_n)$, where S_n is the neutron separation energy of the CN and A is the mass number of the target nucleus in the neutron-induced reaction. Surrogate reactions were first used to infer neutron-induced fission cross sections $\sigma_{n,f}$ [12]. Several measurements, e.g [13], have shown that the $\sigma_{n,f}$ obtained with eq. (2) (i.e. by multiplying the measured fission probabilities $P_{s,f}$ by σ_{CN}), are in good agreement with directly-measured neutron data. However, the WE approximation fails when applied to

infer $\sigma_{n,f}$ of even-even fissioning nuclei [14, 15] and neutron-induced radiative-capture cross sections $\sigma_{n,\gamma}$ [16, 17]. The observed disagreement has been attributed to the differences between the probability distributions F_i populated in the surrogate and neutron-induced reactions and the non-applicability of the WE limit [11]. Recently, Escher et al. [18] and Ratkiewicz et al. [19] have shown that the probabilities for observing specific γ-ray transitions in surrogate reactions combined with the calculated distributions F_s can be used to tune HF model parameters and significantly improve the predictions for $\sigma_{n,\gamma}$ of A ≈ 90 nuclei.

We have recently made an important step forward and applied the surrogate-reaction method to infer both the neutron-induced fission (n,f) and radiative capture cross sections (n,γ) of ^{239}Pu [20]. This was achieved by combining simultaneously-measured fission and γ-emission probabilities ($P_{s,f}$ and $P_{s,\gamma}$) for the ^{240}Pu(^{4}He,^{4}He')^{240}Pu* surrogate reaction with a calculation of the J^π distributions populated in this reaction (F_s in eq. (1)). The latter distributions were obtained with the microscopic reaction model described in [21]. The simultaneous measurement of the decay probabilities of all open decay channels below S_n, allowed us to define with much better precision the set of parameters that describe the de-excitation process, namely the fission-barrier, level-density and γ-ray strength-function parameters. Moreover, measuring the decay probabilities for all the open decay channels also provided a strong test of the experimental technique, because the probabilities must add up to 1 [20]. With our data we were able to determine the first fission-barrier height of the ^{240}Pu nucleus with an uncertainty of only 20 keV, much lower than the typical uncertainty of fission barriers of 100-200 keV. The relative uncertainties of the resulting neutron-induced cross sections of ^{239}Pu vary between 5 and 20%, depending on the neutron energy [20].

Surrogate-reaction experiments in direct kinematics, like the one carried out in [20], have significant limitations. When the nuclei of interest are highly radioactive, the necessary targets are unavailable. In addition, competing reactions in target contaminants (e.g. oxygen) and backings produce a high background, which is very complicated or even impossible to remove. The heavy products of the decay of the compound nucleus are stopped in the target sample and cannot be detected. Therefore, the measurement of γ- and neutron-emission probabilities requires detecting the emitted γ rays and neutrons, which is rather difficult due to the very low detection efficiencies [22].

Using the surrogate-reaction method in inverse kinematics enables for the formation of very short-lived nuclei and for the detection of the heavy, beam-like residues produced after the emission of γ-rays and neutrons. However, the decay probabilities $P_{s,\chi}$ change very rapidly with excitation energy at S_n and at the fission threshold. The excitation-energy resolution required to scan this rapid evolution is a few 100 keV, which is quite difficult to achieve for heavy nuclei in inverse kinematics, due to long-standing target issues. Namely, the required large target density and thickness lead to significant energy loss and straggling effects that translate into a large uncertainty for the energy of the projectile and for the emission angle and the energy of the target-like residue. In addition, the presence of target windows and impurities induces background.

1.3 Surrogate reactions at storage rings

In this work, we address the discussed target issues by investigating for the first time surrogate reactions at the heavy-ion storage rings of GSI/FAIR [23, 24], which offer unique possibilities for the study of nuclear reactions [25].

A key capability of storage rings is beam cooling, which allows for a significant reduction of the size and energy spread of the stored beam. If a gas target is present in the ring, the electron cooler can compensate the energy loss as well as the energy and angular straggling of the beam in the gas target. The heavy ions pass the target always with the same energy and the same outstanding beam quality. Hence, energy loss and straggling effects in the target are negligible, quite in contrast to single-pass experiments. Moreover, the frequent passing of the target zone (about 1 million times per second at 10 AMeV) allows gas targets with ultra-low density (10^{13} atoms/cm^2) to be used and no windows are necessary. This is a great improvement for surrogate reactions since the beam will only interact with the desired material and in a well-defined interaction zone, while the luminosity remains at a high level.

Storage rings can be used to reduce the energy of the stored beam from a few 100 AMeV, the typical energy required to produce bare ions, to a few AMeV. This enables another unique feature: the production of 10 AMeV cooled beams of fully-stripped radioactive heavy ions. Therefore, we do not have to deal with the intense background of beam ions produced after e^- stripping reactions in the target. Moreover, since the gas target has a very low density, the probability for having two successive reactions in the target, a nuclear reaction followed by an atomic reaction and vice versa, is extremely low. Therefore, the beam-like residues produced by the nuclear reaction will also be fully stripped.

However, heavy-ion storage rings are operated in ultra-high vacuum (UHV) conditions (10^{-10} to 10^{-11} mbar), which poses severe constraints to in-ring detection systems. UHV-compatible silicon detectors have only started to be used since a few years for the study of nuclear reactions at the ESR [26, 27].

2 First proof of principle experiment

We have started our program of measurements with a first proof-of-principle experiment at the ESR storage ring. The experiment took place end of June 2022. In this experiment, a ^{208}Pb^{82+} beam at 30.77 AMeV interacted with a gas-jet target of hydrogen. We had on average $5\cdot10^7$ ^{208}Pb^{82+} ions cooled and decelerated per

injection and the target thickness was $6 \cdot 10^{13}$ atoms/cm^2. The ^{208}Pb projectiles were excited by inelastic scattering reactions with the target. We measured the inelastically scattered protons with a Si telescope and the beam residues produced after the de-excitation of ^{208}Pb* via γ-rays and neutron emission with a position-sensitive Si strip detector placed behind one of the magnetic dipoles of the ring, see Fig. 2. The ring dipole magnet downstream from the target acted as a recoil spectrometer separating the unreacted beam, the ^{208}Pb^{82+}residues produced after γ-ray emission and the ^{207}Pb^{82+} residues produced after neutron emission. The beam residues produced after e$^-$ capture in the target were not an issue, because they have a smaller charge, i.e. a larger magnetic rigidity, and were bent outside the ring, far from the γ and neutron-emission residues.

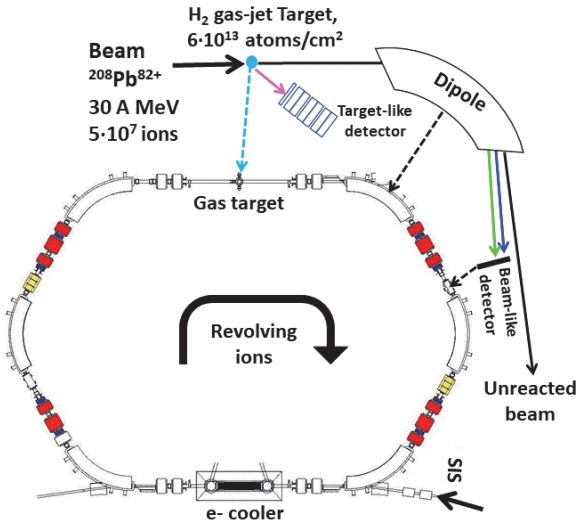

Fig. 2. The lower part shows a schematic view of the ESR. The upper part shows the setup for our proof of principle experiment. The trajectory of the scattered protons is shown in pink and the one of the beam in black. The trajectories of the heavy beam-like residues produced after emission of γ rays (^{208}Pb^{82+}) and a neutron (^{207}Pb^{82+}) are shown in blue and green, respectively.

The telescope was centered at 60° with respect to the beam axis. To prevent the detector components from degrading the UHV of the ring, the telescope was housed in a pocket with a stainless-steel window of 25 µm and operated in air at atmospheric pressure. The distance from the pocket window to the target was 96 mm. The position of this pocket was chosen to avoid interception of the beam. The telescope consisted of one 530 µm-thick DSSSD of 20×20 mm^2 with 16 front strips and 16 back strips at a pitch of 1250 µm, which enabled for the measurement of the energy loss and the collection of angular information. The DSSSD was followed by six single sided, single area detectors for full energy measurements. Each of the latter detectors had an active area of 20×20 mm^2 and a thickness of 1.51 mm. Thus, the total thickness of the telescope was 9.6 mm. This was sufficient to stop scattered protons of up to 43 MeV.

The beam-like residue detector was a DSSSD with a thickness of 500 µm, an active area of 122×44 mm^2, 122 vertical strips and 40 horizontal strips. This detector was also placed inside a pocket and separated from the UHV by a thin stainless-steel window of 25 µm. The pocket was in a movable drive. For each ion-bunch injection in the ESR, the pocket was moved in after cooling and deceleration of the beam, and moved out at the end of the measurement cycle. This allowed us to protect the detector from possible accidental interactions with the uncooled beam. When moved in, this detector was placed at 13.4 mm from the beam axis. With this distance we ensured that the rate of elastic scattered beam ions over the whole detector was well within the expected radiation-damage tolerance range of the detector, which remained operational during the full experiment

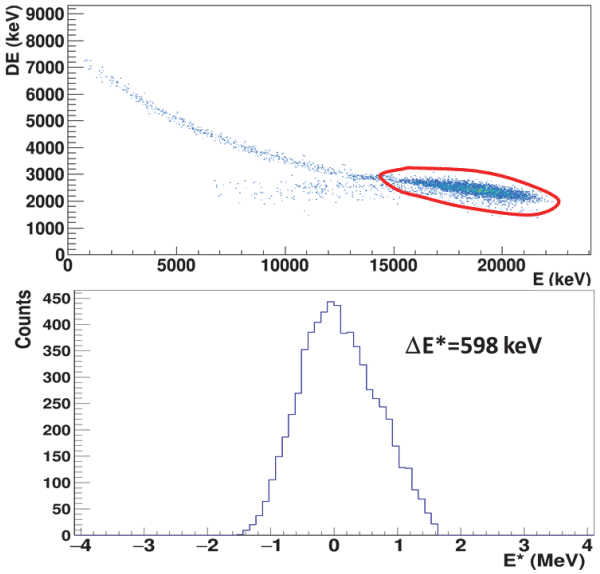

Fig. 3. (Top) Preliminary results for the energy loss versus residual energy of scattered protons detected in one telescope strip at 64.5°. The red contour selects the elastically scattered protons. (Bottom) Preliminary results for the excitation energy of ^{208}Pb for elastically scattered protons. The standard deviation of the peak is indicated.

2.1 Preliminary results

One of the main objectives of this experiment was to evaluate the E* resolution. The upper part of Fig. 3 shows E_{loss}, the energy deposited in the DSSSD of the telescope, versus E_{res}, the sum of the energy deposited in each single-sided thick detector, for protons detected in one strip of DSSSD at 64.5°. The ground state of ^{208}Pb is well separated and can be used to evaluate the excitation energy resolution. This is shown on the lower part of Fig. 3, where the excitation energy spectrum of ^{208}Pb for elastically scattered protons is represented. The upper histogram in Fig. 3 has been corrected for discontinuities above $E_{res} \approx 12$ MeV due to the electronic threshold and the presence of an undepleted region in the interface between first and the second thick detector. The standard deviation of the ground-sate peak is E* ≈ 600 keV. This resolution agrees with our expectations and is dominated by the angular uncertainty of the scattered protons caused by the large target radius of 2.5 mm. Thanks to this first experiment we have been able

to validate our simulations, which we can now use to predict the excitation energy resolution that we would have with a thinner target radius of 1 or 0.5 mm. With such radii, we would have an excitation energy resolution of 300 keV and 200 keV, respectively, for ^{208}Pb using the same set-up. A target with a smaller radius will be available at the ESR for our next experiments.

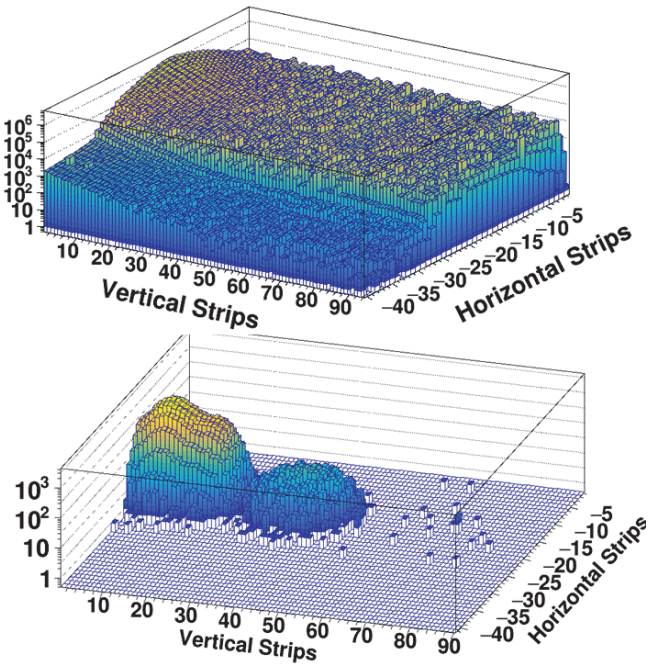

Fig. 4. Preliminary results showing the measured position of beam residues without (top) and with (bottom) coincidence with the scattered protons detected by the telescope. In the bottom figure, $^{208}Pb^{82+}$ nuclei that de-excite by γ emission are in the left bump, while $^{207}Pb^{82+}$ nuclei produced after neutron emission are located in the right bump.

The other main objective of this proof-of-principle experiment was to evaluate the transmission and the separation of the heavy, beam-like residues. Fig. 4 shows the position spectra of heavy residues detected without (top) and with (bottom) the coincidence with the protons detected in the telescope. The heavy residues of the projectile produced after its de-excitation can only be seen in the coincidence spectrum: $^{208}Pb^{82+}$ nuclei that de-excite by γ emission are in the left bump, while $^{207}Pb^{82+}$ nuclei produced after neutron emission are located in the right bump. Therefore, thanks to the detection in coincidence with the protons, we have been able to extract the heavy residues from the very intense background created by the elastic scattering of the beam, which can be seen in the upper part of Fig. 4. Moreover, we can see a very clear separation of the two bumps.

As expected, the beam residues are detected with very high efficiencies. Our preliminary analysis shows that we detect 100% of the residues produced after neutron emission and between 73 to 96% of the residues produced after γ-ray emission. These efficiencies are much larger than what can be obtained in standard surrogate-reaction experiments in direct kinematics [22]. We have determined the efficiencies with simulations that were validated with the data measured at $E^* < S_n$. At these excitation energies, the efficiency for detecting the residues produced after γ-ray emission can be deduced from the measured data because the γ-ray emission probability is equal to 1.

Figure 5 shows the position of the heavy residues in the detector plane for different intervals of excitation energy E*. In the first plot we only have events in the γ-residue peak because the E* is below the neutron separation energy of ^{208}Pb (S_n=7.37 MeV). As the E* becomes larger than S_n, we start to see events in the neutron-emission peak, which becomes the most intense peak at the largest excitation energies (bottom right plot).

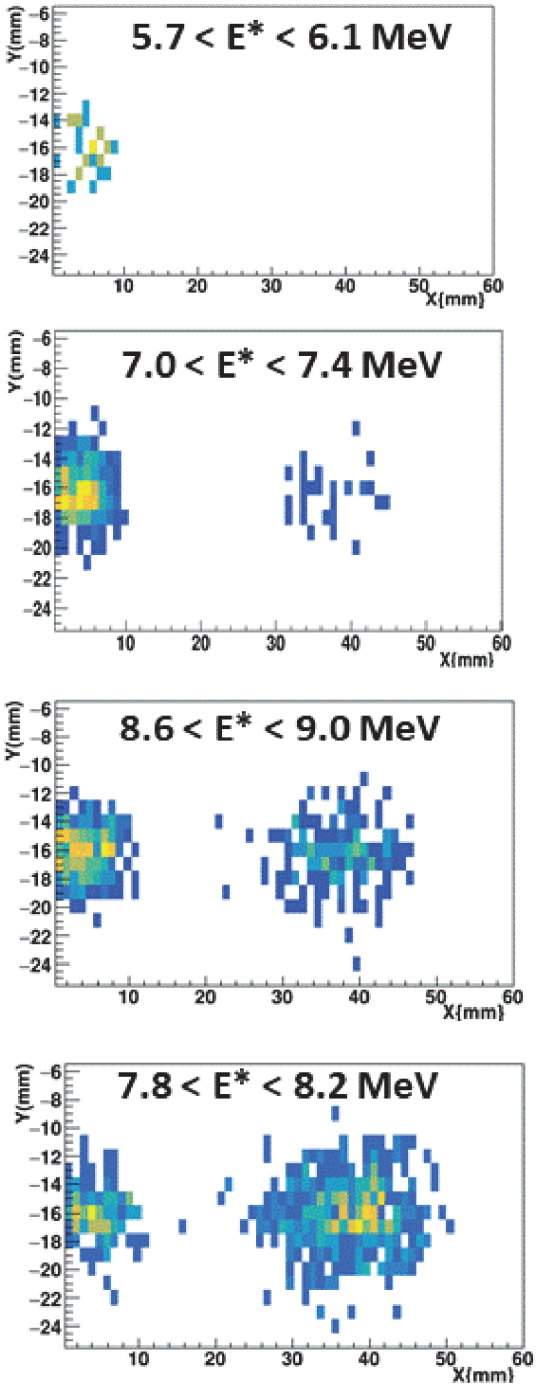

Fig. 5. Preliminary results for the position of heavy residues at the detector plane for different intervals of excitation energy. The corresponding interval is indicated on top of each figure.

By counting events in each of the peaks at different E* intervals, we will be able to extract for the first time simultaneously the γ- and the neutron-emission probabilities of ^{208}Pb. To our knowledge the neutron emission probability as a function of E* has never been measured before for any nucleus.

3 Conclusion and perspectives

The surrogate-reaction method is a powerful tool to infer indirectly neutron-induced cross sections of short-lived nuclei. Heavy-ion storage rings offer ideal conditions to use the surrogate reaction method in inverse kinematics. The beam cooling capabilities of the ring combined with the use of ultra-thin, windowless targets, allow for the determination of the excitation energy with unprecedented resolution. In addition, the magnetic dipoles of the ring enable for the separation of the beam-like reaction residues produced after γ-ray and neutron emission, and their detection with very high efficiencies. In this way, it will be possible to determine simultaneously the decay probabilities of many short-lived nuclei with unrivalled precision.

We successfully conducted a first proof-of-principle experiment at the ESR storage ring. A ^{208}Pb beam interacted elastically and inelastically with a hydrogen gas jet target. With this experiment we were able to evaluate the excitation energy resolution and confirm the full separation and highly efficient detection of the beam-like residues produced after γ and neutron emission. Therefore, this first experiment has allowed us to validate our experimental set-up and our new methodology to infer simultaneously γ- and neutron-emission probabilities.

In the next months, we will complete the data analysis to determine the decay probabilities for γ and neutron emission. These results will be used to fix key model parameters of a HF calculation that includes the calculated spin/parity distributions F_s induced in the ^{208}Pb(p,p') reaction. The latter distributions have been calculated [28]. Once the parameters are fixed, we will use them to calculate the neutron-induced cross sections for radiative capture and inelastic scattering of ^{207}Pb.

In the near future, we plan to perform a second proof of principle experiment with a $^{238}U^{92+}$ beam and a deuterium target. We will investigate the ^{238}U(d,d')^{238}U* and the ^{238}U(d,p)^{239}U* surrogate reactions by measuring, in addition to the γ-ray and neutron emission probabilities, the fission probabilities of ^{238}U and ^{239}U. For this purpose, we will complete the setup used in the first proof-of-principle experiment with fission detectors. To our knowledge, it will be the first time that a fission reaction is studied in a storage ring.

After validation of the experimental method with the proof-of-principle experiments, we foresee to pursue our surrogate-reaction studies at the CRYRING storage ring [24]. Detectors for target-like reaction products and fission fragments are to be installed in a dedicated reaction chamber in the target section of CRYRING, while a detection setup for heavy beam-like residues is to be installed at the focal point placed after the two dipoles downstream from the target section. The installation of a dedicated reaction chamber surrounding the target will allow us to increase the solid angle for the detection of target residues by a factor of about 40. The detection of the beam-like residues at the focal point ensures an optimum separation of the beam-like residues independently from their angular distribution.

Our ultimate goal is to indirectly infer the neutron-induced reaction cross sections of many short-lived nuclides in different regions of the chart of nuclei. First, we will use primary beams of e.g. ^{238}U and ^{208}Pb and nearby secondary beams produced by fragmentation. In the longer term, we aim to explore the region of neutron-deficient actinides and pre-actinides towards the N=126 shell closure. It will be the first time that fission probabilities are measured near a shell closure. This is particularly interesting since the low density of states typical of near-closed-shell nuclei can significantly impact their decay probabilities. These systematic studies will help to provide much better theoretical predictions for the fission barriers and cross sections of neutron-rich nuclei towards the shell closure at N=184, which are essential for the r-process [5, 6] and not yet accessible to experiments.

Acknowledgements

This work is supported by the European Research Council (ERC) under the European Union's Horizon 2020 research and innovation programme (ERC-Advanced grant NECTAR, grant agreement No 884715). We thank the Prime 80 program from the CNRS for funding the PhD thesis of MS and the GSI/IN2P3 collaboration 19-80. AH is grateful for funding from the Knut and Alice Wallenberg Foundation under KAW 2020.0076.

1. B. P. Abbott et al., Phys. Rev. Lett. **119**, 161101 (2017).
2. D. M. Siegel, Eur. Phys. J. A **55**, 203 (2019).
3. D. Watson et al., Nature **574**, 497 (2019).
4. T. Kajino et al., Prog. Part. Nucl. Phys. **107**, 109 (2019).
5. S. Goriely, Eur. Phys. J. A **51**, 22 (2015).
6. N. Vassh et al., J. Phys. G: Nucl. Part. Phys. **46**, 065202 (2019).
7. Y. L. Zhu et al., Astrophys. J. **906**, 94 (2021).
8. N. Colonna et al., Energy Environ. Sci. **3**, 1910 (2010).
9. M. Arnould et al., Phys. Reports **450**, 97 (2007).
10. N. Bohr, Nature **137**, 344 (1936).
11. J.E. Escher et al., Rev. Mod. Phys. **84**, 353 (2012).

12. J. D. Cramer and H. C. Britt, Phys. Rev. C **2**, 2350 (1970).
13. G. Kessedjian et al., Phys. Lett. B **692**, 297 (2010).
14. W. Younes and H. C. Britt, Phys. Rev. C **67**, 024610 (2003).
15. O. Bouland, Phys. Rev. C **100**, 064611 (2019).
16. G. Boutoux et al., Phys. Lett. B. **712**, 319 (2012).
17. Q. Ducasse et al., Phys. Rev. C **94**, 024614 (2016).
18. J. E. Escher et al., Phys. Rev. Lett. **121**, 052501 (2018).
19. A. Ratkiewicz et al., Phys Rev Lett. **122**, 052502 (2019).
20. R. Pérez Sánchez et al., Phys. Rev. Lett. **125**, 122502 (2020).
21. M. Dupuis et al., Eur. Phys. J A **51** (2015) 168.
22. R. Pérez Sánchez et al., Nucl. Instr. Meth. A **933**, 63 (2019).
23. B. Franzke, Nucl. Instrum. Methods B **25**, 18 (1987).
24. M. Lestinsky et al., Eur. Phys. J. Special Topics **225,** 797 (2016).
25. M. Steck et al., Prog. Part. Nucl. Phys. **115**, 103811 (2020).
26. J. C. Zamora et al., Phys. Rev. C **96**, 034617 (2017).
27. J. Glorius et al., Phys Rev Lett **122**, 092701 (2019).
28. M. Dupuis, private communication (2022).